


Terahertz conductivity and coupling between geometrical and plasmonic resonances in nanostructures

Jiří Kuchařík and Hynek Němec*

Institute of Physics, Czech Academy of Sciences, Na Slovance 2, 18221 Prague 8, Czech Republic

Tomáš Ostatnický

Faculty of Mathematics and Physics, Charles University, Ke Karlovu 3, 12116 Prague 2, Czech Republic

 (Received 12 July 2017; revised manuscript received 12 December 2018; published 3 January 2019)

Terahertz conductivity spectra of charges moving ballistically in one-, two-, and three-dimensional infinitely deep rectangular potential wells were investigated theoretically using semiclassical and quantum Kubo formulas. The conductivity spectrum of a degenerate electron gas in these nanostructures exhibits a series of geometrical resonances. These further couple with plasmon resonances occurring in isolated structures: qualitatively different interaction regimes are found in one-, two-, and three-dimensional nanostructures. In contrast, the response of a nondegenerate electron gas smears into a single broad band due to the excessive spectral broadening caused by the wide distribution of charge velocities.

DOI: [10.1103/PhysRevB.99.035407](https://doi.org/10.1103/PhysRevB.99.035407)

I. INTRODUCTION

For decades, semiconductor and metallic nanostructures have constituted an important field for understanding electronic properties of materials under well-defined conditions. Most works concentrate on the investigation of complex quantum phenomena which are inherently linked with intense magnetic fields; dc conduction is then usually measured to assess the role of these effects [1,2]. The high-frequency conductivity has been intensively investigated, namely, in metallic nanoparticles, where a strong broad plasma resonance typically dominates over the influence of the electron confinement [3,4]. However, less attention has been devoted to the response of semiconductor nanostructures where confinement effects and plasma oscillations may be equally important [5]. On the one hand, there are a number of experimental works reporting that the conductivity spectra of a large variety of semiconductor nanostructures universally contain just a single very broad resonance, which can be—at least qualitatively—reproduced using the phenomenological Drude-Smith model [6–11]. The underlying charge transport is essentially ballistic, because the mean free path between bulk scattering events is typically longer than the size of these nanostructures. On the other hand, theoretical investigations of ballistic motion in a variety of systems including nanodiscs [12,13] and chaotic billiards [14] demonstrate conductivity spectra with distinct spectral features. Sharp spectral features were experimentally observed, for example, in patterned two-dimensional electron gases (2DEGs) [15,16]. In order to synthesize these strikingly different results, a general overview of involved processes and properties is required. The ability to interpret the high-frequency response is even more important since the conductivity spectra contain information on charge transport mechanisms and related parameters in nanomaterials.

A thorough understanding of charge motion and response in nanostructures may stimulate a development of ultrafast nanocomponents with new functionalities. The resonant behavior described in this paper may inspire, e.g., a design of narrow-band antennae.

While theoretical approaches for determining the optical response of semiconductor nanostructures are well established at various levels of accuracy and complexity, calculations of the response in the terahertz (THz) range still remain challenging. The existing semiclassical approach requires the use of time-consuming Monte Carlo calculations [17], and it was only recently that a simple analytical formula capturing the main aspects of the response of a confined nondegenerate electron gas was reported [18]. Quantum-mechanical calculations using directly the Kubo-Greenwood formula within the common relaxation-time approximation (e.g., Ref. [19]) are conceptually straightforward. However, this simple approach fails since it incorrectly yields a nonzero dc conductivity in isolated nanostructures (while it is obvious that no steady current can flow across a finite isolated object), which inevitably infracts also the rest of the THz conductivity spectrum [20]. The main reason for this behavior is broken translational symmetry: in the common relaxation-time approximation, the charge density displaced by the probing electric field is instantaneously returned back to the equilibrium (homogeneous distribution) upon scattering, while the corresponding current is completely omitted (this is not an issue in translationally invariant systems where charge neutrality is preserved at any time). Evaluation of this restoring thermalization current (which is of a diffusion nature in reality) is then required to obtain physically correct results [20]. The influence of this restoring current is particularly important for lower frequencies and larger nanostructures considered here.

In this paper, we focus on the simplest possible scenario—ballistic (or close to ballistic) motion of noninteracting charges in a multidimensional infinite rectangular potential well. The simplicity of the mathematical solution allows

*Corresponding author: nemec@fzu.cz

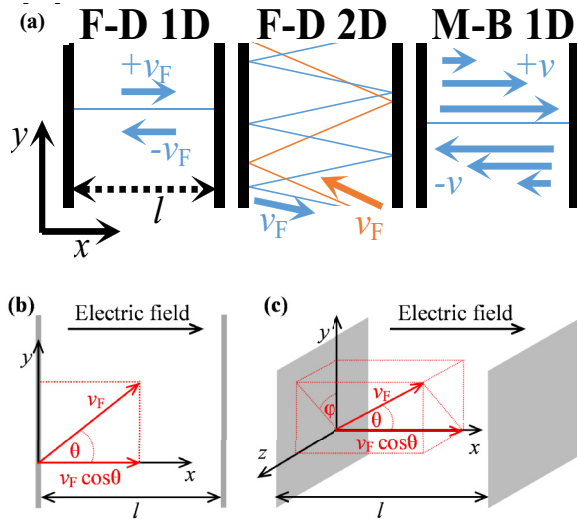


FIG. 1. (a) Schematics of the charge motion in the studied rectangular potential wells for Fermi-Dirac (F-D) and Maxwell-Boltzmann (M-B) statistics. Note that the presence/absence of the enclosure in the y direction of the 2D structure does not affect its response in the x direction since the x -velocity component is preserved upon elastic specular reflections at these boundaries. (b), (c) Geometries used for the derivation of mobility of charges bouncing between two straight parallel planes in two and three dimensions.

examination of the conditions under which distinct spectral features may be observed. Although sharp spectral lines are usually associated with well-defined quantum transitions in small nanoparticles, we show theoretically that pronounced spectral features can emerge in THz conductivity spectra even for larger particles for which the semiclassical limit applies (Sec. II). In order to assess the limits of validity of the semiclassical approach, we also investigate the response using quantum mechanics (Sec. III). The principal result of this paper is then the demonstration of uncommon interaction between geometrical resonances in degenerate electron gas with plasma oscillations (Sec. IV). We conclude that in one- and two-dimensional structures this coupling is qualitatively different from that encountered for nondegenerate plasmas.

II. SEMICLASSICAL CALCULATIONS

Our theoretical analysis is based on the semiclassical Kubo formula [21] for the mobility tensor:

$$\mu_{jk}(f) = e_0 \mathcal{N} \int_0^\infty \langle v_j(0) v_k(t) \rangle e^{2\pi i f t} dt, \quad (1)$$

where e_0 is the elementary charge, $v_k(t)$ are the components of charge thermal velocity evolving according to Newton's equations of motion, and f is the frequency conjugate to the time t . The averaging $\langle \dots \rangle$ takes place over trajectories with initial states weighted by $-\partial F(E)/\partial E$, where $F(E)$ is the distribution function. The normalization factor $\mathcal{N} = 1/\int G(E)F(E)dE$ [$g(E)$ is the density of states] simplifies to $1/(k_B T)$ for Maxwell-Boltzmann distribution, and to $D/(2E_F)$ for Fermi-Dirac distribution with Fermi energy E_F in a D -dimensional space when $k_B T \ll E_F$. We consider

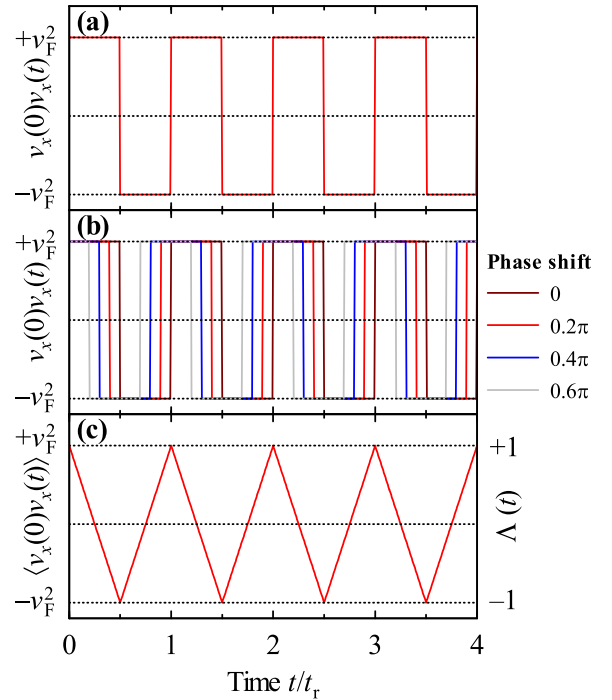


FIG. 2. Illustration of the derivation of the autocorrelation function for 1D bouncing between straight parallel planes. (a) For a single charge, the product $v_x(0)v_x(t)$ takes the form of a square wave with phase shift determined by the initial charge position. (b) The averaging in the autocorrelation function takes place over all possible initial positions, which are represented by different phase shifts (a few of them are illustrated in the graph). (c) After integration over all possible initial phases of motion, we obtain the triangle wave shape of the autocorrelation function.

long bulk scattering times (e.g., electron mobility of $2.4 \times 10^5 \text{ cm}^2 \text{ V}^{-1} \text{ s}^{-1}$ corresponding to bulk scattering time of 10 ps was reported in high-quality GaAs in Ref. [22]), as they favor the role of interaction of carriers with nanostructure boundaries over bulk scattering. We assume that the reflection of carriers upon reaching the nanostructure boundary is elastic and specular, thus neglecting the possible influence of surface roughness [12]. In all illustrations, we assume that the carriers have an effective mass $m = 0.07m_e$ as in GaAs.

We start with the simplest one-dimensional (1D) model in which carriers bounce between two straight parallel planes at normal incidence [Fig. 1(a)]. This prototype enables understanding of the response of more complex systems; furthermore, it directly describes the longitudinal response of charges in quantum wires. In the limit $T \rightarrow 0 \text{ K}$, $-\partial f/\partial E$ reduces to the Dirac delta function, therefore only charges initially moving with Fermi velocity v_F contribute to the statistical average $\langle \dots \rangle$ in Eq. (1). This means that the carrier velocity v_x periodically switches between $+v_F$ and $-v_F$ as the carrier reflects from the planes; the period of this motion is the round-trip time $t_r = 2l/v_F$, where l is the distance between the planes. The product $v_x(0)v_x(t)$ which appears in the autocorrelation function is thus a square wave oscillating between $\pm v_F^2$ with period t_r [Fig. 2(a)]. Depending on the initial positions in the phase space, the phase shift of this square wave may take any

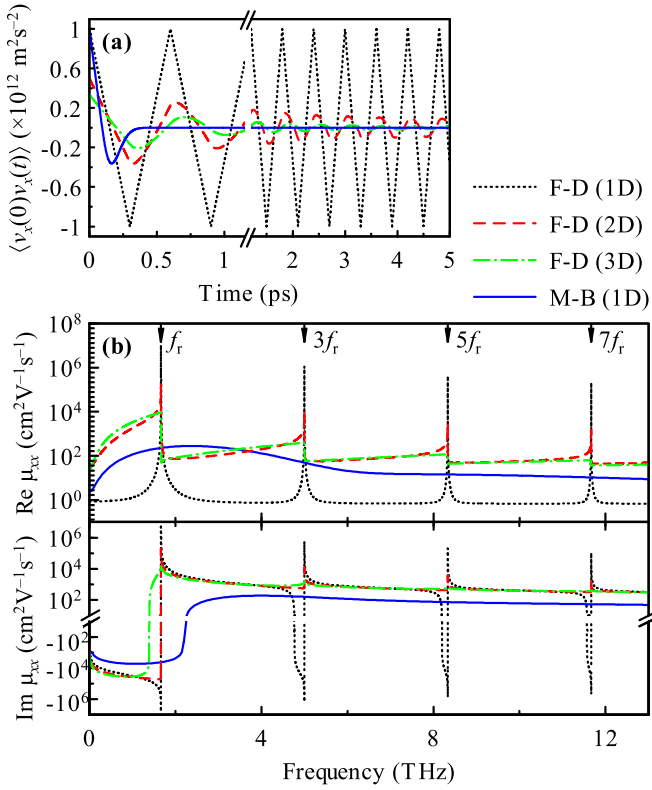


FIG. 3. (a) Velocity autocorrelation functions in the time domain of charges bouncing in a multidimensional infinite rectangular well ($l = 300 \text{ nm}$). The carriers were described either with Fermi-Dirac statistics (F-D) ($v_F = 1000 \text{ nm/ps}$, $E_F = 0.20 \text{ eV}$, $T = 0 \text{ K}$) or Maxwell-Boltzmann statistics (M-B) (to permit the comparison at the same frequency scale, the mean square velocity is set to be equal to v_F^2 , i.e., formally $T = 4620 \text{ K}$; to transfer the results towards realistic temperatures, the frequency would need to be scaled with \sqrt{T}). (b) Corresponding mobility spectra calculated using the Kubo formula. For the purpose of plotting, we phenomenologically introduced a bulk scattering time $\tau_s = 1 \text{ ns}$ [the velocity autocorrelation function is multiplied by $\exp(-t/\tau_s)$]; this replaces the δ functions by narrow Lorentzians in the case of 1D Fermi-Dirac statistics and prevents divergences in its 2D variant. This unrealistically long scattering time permits a clear distinction of the intrinsic damping in the 2D and 3D system (picosecond time scale) from the artificial extrinsic losses (1-ns decay time).

value just from the interval $(0, \pi)$, since the value at zero time $v_x^2(0)$ is always positive [Fig. 2(b)]. Averaging over all possible initial positions then directly yields a triangle wave $\Lambda(t/t_r)$ [Figs. 2(c) and 3(a)], where the symbol $\Lambda(x)$ denotes a triangle function oscillating between $+1$ and -1 with period 1. Substitution of this result into Kubo formula (1) then yields (without bulk scattering)

$$\text{Re } \mu_{xx}(f) = \frac{e_0}{m} \times \frac{2}{\pi^2} \sum_{k=-\infty}^{\infty} \frac{\delta[f - (2k+1)f_r]}{(2k+1)^2}, \quad (2)$$

$$\text{Im } \mu_{xx}(f) = -\frac{e_0}{m} \times \frac{2}{\pi^3} \sum_{k=-\infty}^{\infty} \frac{1}{f - (2k+1)f_r} \times \frac{1}{(2k+1)^2}. \quad (3)$$

The real part of mobility consists of a sum of Dirac delta functions which are located at the fundamental frequency corresponding to the round-trip movement with frequency $f_r = 1/t_r$ and at its odd harmonics [Fig. 3(b)]. It should be stressed that the resonant frequencies for a given nanowire length l depend only on the Fermi velocity, i.e., they can be tuned by controlling the Fermi level (or equivalently, charge density) of the electron gas. The presence of the harmonic frequencies stems from the anharmonic shape of the confining potential, which leads to an anharmonic character of charge trajectories. In the quantum-mechanical picture, we will later show that these harmonics have an origin in dipolar transitions to higher unoccupied levels.

In the two-dimensional (2D) case, charges can move at an oblique angle θ , therefore the round-trip time is longer compared with the 1D case and it reads $t_r/\cos\theta$. The initial velocity component parallel with the probing electric field is then a projection to the x axis (perpendicular to the confining planes): $v_x(0) = v_F \cos\theta$ [Fig. 1(b)]. Averaging over all initial positions can be done analogically as in the 1D case, resulting in the triangular evolution of the velocity with time:

$$v_F \cos\theta \Lambda\left(\frac{t}{t_r/\cos\theta}\right). \quad (4)$$

Averaging over all possible directions of movement (θ in the interval from zero to 2π) then yields the velocity autocorrelation function in the time domain:

$$\langle v_x(0)v_x(t) \rangle = \frac{\int_0^{2\pi} v_F^2 \cos^2\theta \Lambda\left(\frac{t}{t_r} \cos\theta\right) d\theta}{\int_0^{2\pi} d\theta}, \quad (5)$$

Substitution of this result into Kubo formula (1) and considering that $E_F = m v_F^2/2$ then yields

$$\mu_{xx}(f) = \frac{e_0}{m} \frac{1}{\pi} \int_0^{\infty} e^{2\pi i f t} \int_0^{2\pi} \Lambda\left(\frac{t}{t_r} \cos\theta\right) \cos^2\theta d\theta dt. \quad (6)$$

Analogically as in the case of the 1D problem, the mobility spectrum [Fig. 3(b)] contains a series of odd harmonics with fundamental frequency f_r . The oscillations of the time-domain autocorrelation function (the inner integral) are damped due to dephasing of the triangle functions corresponding to carriers moving under different angles θ [Fig. 3(a)]; this causes an intrinsic broadening of the peaks in the spectrum [Fig. 3(b)], similarly as in the case of nanodiscs [12,13]. The low-frequency tails are due to carriers with nonzero velocity component along the planes: such carriers need a longer time to travel between the planes, which implies a lower bouncing frequency. Since no trajectory has a period shorter than t_r , there is no broadening towards higher frequencies and the diverging conductivity at the frequency $1/t_r$ is followed by a sharp cutoff.

In the three-dimensional (3D) case, the charge velocity has an additional component parallel to the confining surfaces. After transformation to spherical coordinates [Fig. 1(c)], the round-trip time as well as the x component of the velocity is controlled solely by the polar angle θ , i.e., both quantities are described by identical formulas as in the 2D case. Unlike in the 2D case, the averaging in the time-domain autocorrelation

function consists of the integration over azimuthal and polar angles (φ and θ , respectively) and includes the Jacobian part $\sin \theta$ due to the transformation into spherical coordinates:

$$\langle v_x(0)v_x(t) \rangle = \frac{\int_0^{2\pi} d\varphi \int_0^\pi v_F^2 \cos^2 \theta \Lambda\left(\frac{t}{t_r} \cos \theta\right) \sin \theta d\theta}{\int_0^{2\pi} d\varphi \int_0^\pi \sin \theta d\theta}. \quad (7)$$

The trivial integrations along with the substitution of this result into Kubo formula (1) lead to

$$\mu_{xx}(f) = \frac{3e_0}{2m} \int_0^\infty e^{2\pi i f t} \int_0^\pi \Lambda\left(\frac{t}{t_r} \cos \theta\right) \cos^2 \theta \sin \theta d\theta dt. \quad (8)$$

The additional degree of freedom leads to a broader distribution of velocities in the x direction, causing a faster damping of the oscillations of the time-domain autocorrelation function [Fig. 3(a)]. As a result, the cutoff at the frequency f_r is not preceded by a diverging conductivity; only a discontinuity exists [Fig. 3(b)].

The striking influence of the distribution of velocities is best illustrated in comparison with the motion controlled by Maxwell-Boltzmann statistics (nondegenerate electron gas) in a 1D space. Calculation of the mobility spectrum then involves averaging over the velocity amplitudes:

$$\mu_{xx}(f) = \frac{e_0}{k_B T} \sqrt{\frac{2m}{\pi k_B T}} \int_0^\infty e^{2\pi i f t} \times \int_0^\infty \Lambda\left(\frac{vt}{2l}\right) v^2 \exp\left(-\frac{mv^2}{2k_B T}\right) dv dt. \quad (9)$$

The velocity autocorrelation in the time domain (the inner integral) exhibits very rapidly damped oscillations [Fig. 3(a)]. After the Fourier transform, the resulting spectral shape thus becomes very broad, resembling the Drude-Smith response [Fig. 3(b)]. This behavior emphasizes the key role of the broad velocity distribution: despite the absence of the bulk scattering, the effective damping and the associated resonance width induced by the carrier dephasing are large enough to form a single broad absorption band.

Degeneracy of the electron gas (i.e., $k_B T \ll E_F$) is thus a necessary (although not sufficient) condition for the clear resolution of individual harmonics. In degenerate gases, the response is dominated by charges moving perpendicularly to the surface, whereas the influence of charges moving under an oblique angle θ (and thus contributing to the low-frequency tails) is suppressed by the weight factors $\cos^2 \theta$ and $\cos^2 \theta \sin \theta$ in two and three dimensions, respectively [Eqs. (6) and (8), respectively]. In the nondegenerate case, the entire distribution of velocities contributes already in one dimension: this gives rise to the dominating single broad band. Upon a careful examination it is possible to attribute the weak background above this broad band [frequencies $\gtrsim 6$ THz in Fig. 3(b)] to the onset of the high harmonics.

In real nanomaterials, the spectra are further smeared due to the bulk scattering and due to the inhomogeneous broadening. A bulk scattering time τ_s exceeding one half of the round-trip time t_r is thus another prerequisite for the observation of the high harmonics [Fig. 4]. This condition can be

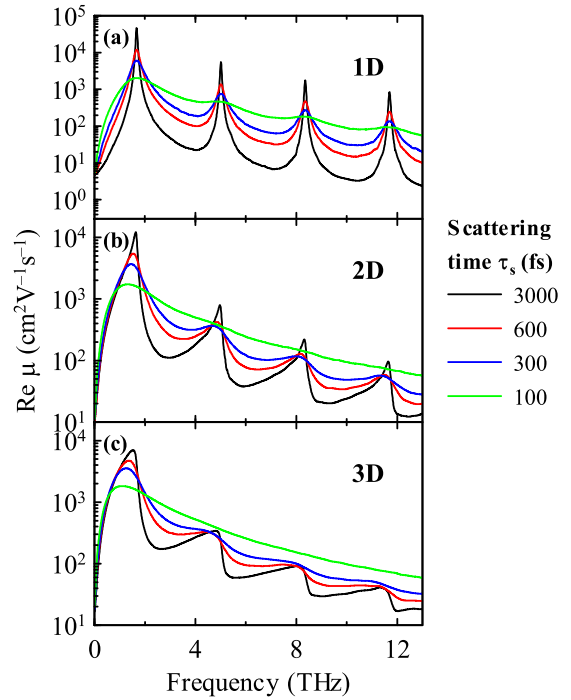


FIG. 4. Calculated mobility spectra of confined degenerate electron gas in the presence of finite bulk scattering ($l = 300$ nm, $v_F = 1000$ nm/ps, $E_F = 0.20$ eV, and $T = 0$ K, i.e., $t_r = 600$ fs). Spectral resonances can be resolved for bulk scattering times as short as one half of the round-trip time t_r .

easily met in 2DEG-based nanostructures at low temperature (long τ_s) or in nanometer-sized metallic particles (short t_r due to the high Fermi velocity). The large spectral separation of the harmonic geometrical resonances also weakens the demand on monodispersity (size distribution with full width reaching 100% of the mean value is acceptable to distinguish the fundamental and third harmonics). Lithography-based methods now routinely provide substantially better structures [16,23].

The calculated mobility spectra of degenerate electron gases depend on the Fermi velocity and, in turn, also on the carrier concentration. In the semiclassical limit (characterized by a continuous density of states), v_F is proportional to $n^{1/D}$. The frequencies of all resonances in these model systems are thus also proportional to $n^{1/D}$, as illustrated in Figs. 5(a)–5(c). We will call these resonances “geometrical,” as the proportionality constant is determined solely by the geometry and scales with the reciprocal nanostructure size. The $1/D$ power dependence on the carrier density is universal; the developed theory thus qualitatively applies for any nanostructure shape.

III. QUANTUM-MECHANICAL APPROACH

The semiclassical calculations from the previous section are important since they allow easy and transparent assessment of the qualitative behavior. However, since we are dealing with nanoscopic physics, we have to check the limits of validity of such description. For this reason, we calculate the conductivity spectra also using the formalism from

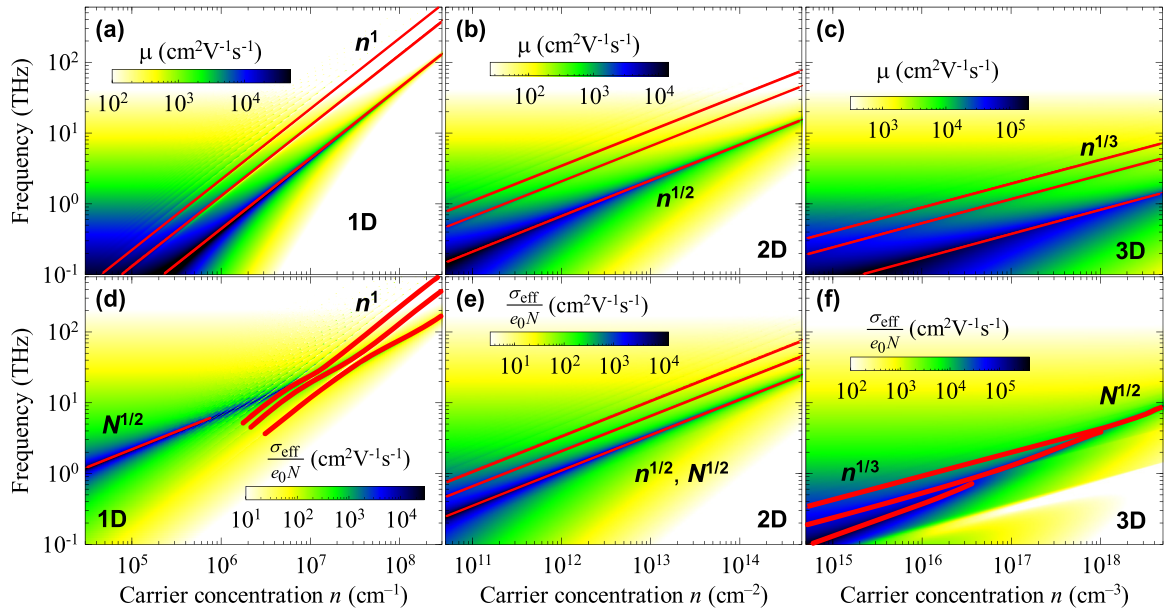


FIG. 5. (a)–(c) Mobilities of D -dimensional degenerate electron gas confined in an infinite rectangular potential well ($l = 300$ nm). (d)–(f) Effective conductivities of mutually isolated nanostructures forming the brick-wall structure shown in Fig. 7. Solid red lines serve as a guide for the eye to indicate the behavior of a few lowest resonances: The parts of the curves following the $N^{1/2}$ trend represent the plasmonic resonance whereas those with the $n^{1/D}$ dependence represent the geometrical resonances. For the purpose of plotting, bulk scattering time $\tau_s = 10$ ps was considered. The density of nanowires in (d) is $\eta_1 = 10^{12}$ cm $^{-2}$, and the density of nanosheets in (e) is $\eta_2 = 10^5$ cm $^{-2}$. The filling factor is $s = 0.5$ in panels (d) and (e), and $s = 0.944$ in panel (f). All panels show the amplitudes of the complex spectra.

Ref. [20] which is based on the Kubo-Greenwood formula within relaxation-time approximation, and which accounts for the restoring thermalization current, thus ensuring a correct and physical shape of the resulting spectra.

In general, there are two aspects which need to be addressed. First, the size of the nanostructure should significantly exceed the de Broglie wavelength of electrons at Fermi level, which requires $v_F \gg h/(ml)$, i.e., the calculations are applicable only for sufficiently high carrier concentrations [$n \gg 8\pi/(3l^3) = 3 \times 10^{14}$ cm $^{-3}$, $n \gg 2\pi/l^2 = 7 \times 10^9$ cm $^{-2}$, and $n \gg 4/l = 1 \times 10^5$ cm $^{-1}$ in 3D, 2D, and 1D potential wells with size $l = 300$ nm]. Second, the quantum transitions should be smeared enough so that the density of states (DOS) could be regarded as a continuum (this can be generally assured using a scattering h/τ_s stronger than the energy-level spacing around E_F).

In Fig. 6 it is illustrated that even close to these critical concentrations the first geometrical resonance is clearly resolved in the quantum-mechanical results, and its frequency coincides with that obtained using the semiclassical calculations (the match becomes almost perfect for higher carrier densities). Higher-order geometrical resonances (which are easily identified in the semiclassical approximation) become resolvable at somewhat higher carrier densities. The discrete nature of the DOS causes splitting of the corresponding peaks—this effect is suppressed either upon increasing carrier density or upon using a stronger damping which would smear the individual transition lines. In this sense, the existence of the higher-order geometrical resonances is confirmed also in the quantum-mechanical view. Note that the differences between quantum and semiclassical approach are less important for 3D systems, as their DOS is higher.

The origin of the peaks predicted by semiclassical calculations can be justified as follows. Quantum energy levels E_p in an infinitely deep rectangular potential well read

$$E_p = \frac{\pi^2 \hbar^2 p^2}{2ml^2}, \quad (10)$$

where p is a positive integer. Selection rules of a dipole approximation allow transitions to levels $q = p + 1 + 2k$, where k is a non-negative integer. The frequency $f_{p \rightarrow q}$ of such a transition is

$$f_{p \rightarrow q} = \frac{E_q - E_p}{2\pi \hbar} = \frac{\pi \hbar}{4ml^2} (2p + 2k + 1)(2k + 1). \quad (11)$$

At zero temperature, states are occupied up to the Fermi energy, which determines the highest occupied energy level p . A large structure size l means that the states are dense and approach the continuum; degeneracy of electron gas then implies that Fermi energy corresponds to a high value of p . Dipole matrix elements rapidly decrease with increasing k , therefore only transitions close to the Fermi level (both p and q are close to the Fermi energy, and thus $k \ll p, q$) contribute to the response. In Eq. (11) we can thus approximate $2p + 2k + 1$ by $2p$ and obtain

$$f_{p \rightarrow q} \approx \frac{v_F}{2l} (2k + 1), \quad (12)$$

which is equivalent with the semiclassical result. The harmonics accompanying the semiclassical motion thus have their origin in quantum transitions to higher energy levels.

The main conclusion of this part is that the semiclassical description of the THz response of larger nanostructures

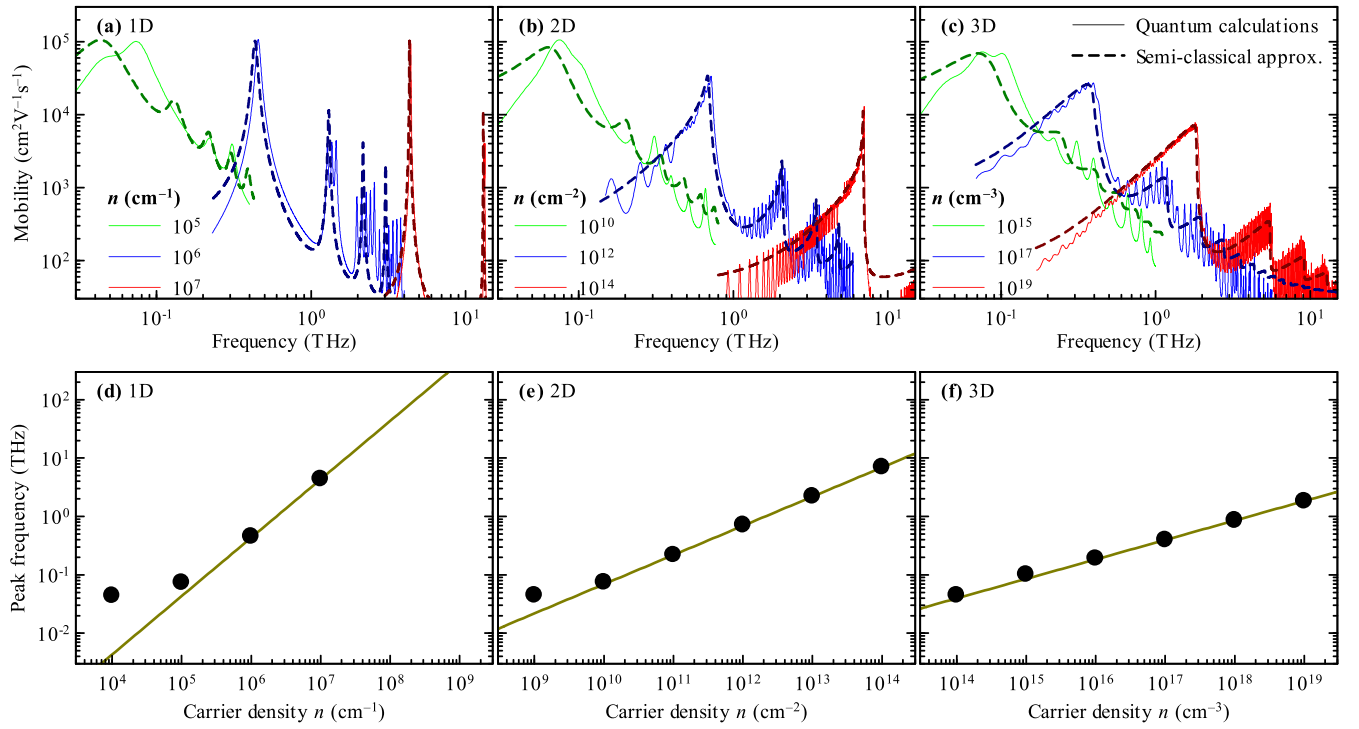


FIG. 6. (a)–(c) Comparison of real parts of mobility spectra calculated using the quantum-mechanical approach described in Sec. III (thin solid lines) and using the semiclassical approximation introduced in Sec. II (thick dashed lines) for various carrier concentrations. (d)–(f) Comparison of the frequency of the first peak from panels (a)–(c) (symbols) and position of the fundamental geometrical resonance calculated semiclassically (lines). Parameters: $l = 300$ nm, $v_F = 1000$ nm/ps ($E_F = 0.20$ eV), $T = 0$ K, and $\tau_s = 10$ ps.

captures the fundamental physical picture. In order to keep our considerations as simple as possible, we will thus keep using the semiclassical treatment in the next section.

IV. PLASMONIC RESONANCE

It should be stressed that the calculated conductivities so far describe the response to the local probing electric field. However, almost all nanostructures are embedded in a surrounding environment, thus forming an inherently heterogeneous system where depolarization fields cause the local field to be screened and thus to be different from the applied one: the measured (effective) conductivity spectrum then generally differs from the local one [5].

We consider a periodic structure consisting of alternating conductive and nonconductive blocks [Fig. 7], which we treat with effective medium theory based on a brick-wall model [24]. In Ref. [5], it was demonstrated that the existence and behavior of a plasmonic resonance are essentially a consequence of a nonexistent percolation pathway in the direction of the polarization of the driving ac field. For this reason, we limit ourselves to this simplest geometry as qualitatively identical results would be obtained in any other geometry with non-percolated conductive blocks. We thus consider the structures sketched in Figs. 7(a)–7(c), which are composed of blocks filled with the nanostructures (surrounded by infinitesimally thin isolating barriers) separated by insulating layers with finite thickness. Obviously, there is no percolation pathway in the direction of the probing electric field (x direction). The symmetry ensures that an x -polarized field does not induce

a net electric field in the y and z directions; this situation is equivalent to the one described within the brick-wall effective medium model [Fig. 7(d)]. The number of nanosheets per unit length η_2 and the number of nanowires per unit area η_1 are then additional parameters entering the calculations: these— together with the carrier density in the nanostructures— control at which (volume) density the crossover between the plasmonic and geometrical resonance occurs.

We assume that the nonconductive parts have a purely real permittivity ε_1 while the permittivity ε_2 of the conductive parts includes the conduction response: $\varepsilon_2 = \varepsilon_1 + ieN\mu_{xx}(f, n)/(2\pi f\varepsilon_0)$. The symbol N stands for the average number of charges per unit *volume* of the block, whereas the symbol n expresses the number of charges per unit *length*, *surface*, and *volume* for one, two, and three dimensions, respectively. Obviously, $N = n$ for 3D nanostructures, whereas $N = \eta_2 n$ for 2D nanostructures and $N = \eta_1 n$ for 1D nanostructures. Denoting s as the filling fraction of the conducting parts, the effective permittivity ε_{eff} is determined from

$$\frac{1}{\varepsilon_{\text{eff}}} = \frac{1-s}{\varepsilon_1} + \frac{s}{\varepsilon_2} \quad (13)$$

and the plasma frequency reads

$$f_{\text{pl}} = \frac{1}{2\pi} \sqrt{\frac{e^2 N(1-s)}{m\varepsilon_0\varepsilon_1}}. \quad (14)$$

The results will be represented in the form of effective conductivity $\sigma_{\text{eff}} = -i\omega\varepsilon_0(\varepsilon_{\text{eff}} - \varepsilon_1)$ normalized by the charge

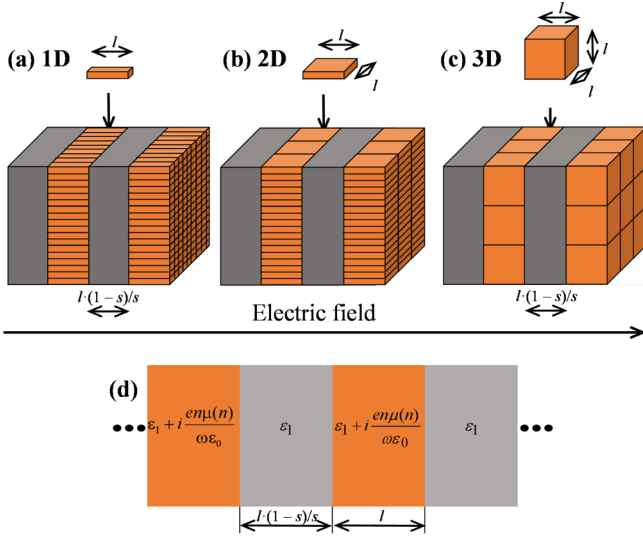


FIG. 7. (a)–(c) Mutually isolated conducting 1D, 2D, or 3D nanostructures (orange) are separated by thick nonconductive parts (gray, permittivity $\epsilon_1 = 12.6$). In this geometry, the percolation along the direction of the probing electric field is broken, which ensures the buildup of the plasmonic resonance. The effective response of all these geometries is equivalent to the structure shown in (d), composed of alternating conducting and nonconductive (laterally infinite) blocks (analogy with capacitors connected in series). To assure the correct filling factor s , the thickness of the isolating block has to be scaled by $(1 - s)/s$ as indicated.

density e_0N [Figs. 5(d)–5(f), 8(c), and 8(d)]. The purpose of this construction is to compare the single-electron responses: note that the ratio $\sigma_{\text{eff}}/(e_0N)$ can be identified with the electron mobility in the case of homogeneous systems.

We first recall the response of large nanostructures (size $l \rightarrow \infty$) for which the bare conductivity approaches the Drude spectrum (characterized by a peak located at zero frequency, independently of the charge density) [Fig. 8(a)]. The effective conductivity then exhibits a plasmonic resonance [Fig. 8(c)] which follows the $N^{1/2}$ density dependence of the plasmon frequency, as discussed, e.g., in Ref. [25].

Analogical behavior is observed for confined nondegenerate electron gas. The geometrical resonance is then carrier-density-independent [Fig. 8(b)]. This resonance dominates in the effective conductivity at low carrier densities, whereas the plasmonic resonance follows the square root of carrier density ($N^{1/2}$) and takes over at higher carrier densities.

The effective conductivity of confined degenerate electron gas in Figs. 5(d)–5(f) exhibits clear signatures of a coupling between the plasmonic resonance (with frequency proportional to $N^{1/2}$) and the geometrical resonances (with frequencies proportional to $n^{1/D}$). In the 3D case [Fig. 5(f)], individual geometrical resonances exist for low carrier concentrations, and they are not influenced by the plasmonic resonance. With increasing carrier concentration, mixing with the plasmonic mode becomes important, and the plasmonic resonance completely takes over at high concentrations. This behavior resembles the coupling of Drude and plasmonic resonance [25], where the Drude peak at zero frequency exists

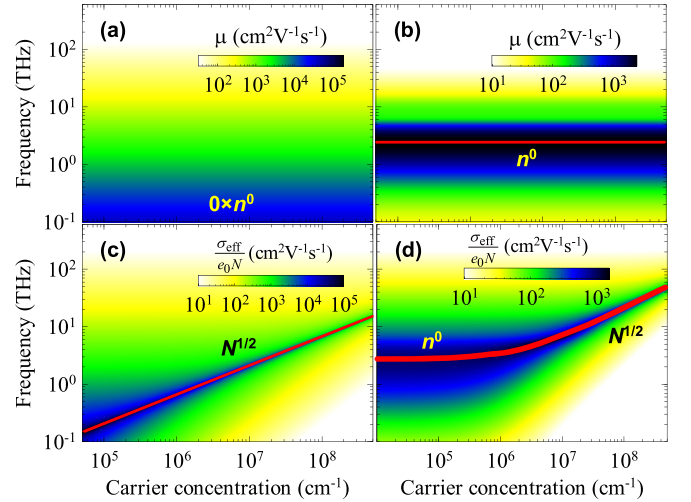


FIG. 8. (a) Drude mobility spectrum (nanostructure size $l \rightarrow \infty$): The Drude peak is located at zero frequency. (b) Mobility spectrum μ_{xx} of nondegenerate electron gas in a 1D nanostructure ($l = 300$ nm) calculated using Eq. (5). (c), (d) Effective conductivities of the structure from Fig. 7(d). Solid red lines serve as a guide for the eye for the resonances: The parts of the curves following the $N^{1/2}$ trend represent the plasmonic resonance. Further parameters: $T = 4620$ K, $\tau_s = 10$ ps, and $s = 0.5$. The density of nanowires in (d) is $\eta_1 = 10^{11}$ cm⁻². All panels show the amplitudes of the complex spectra.

only in the limit of $N \rightarrow 0$ and the plasmonic resonance emerges for a nonzero carrier concentration. In one and two dimensions, however, the behavior is strikingly different.

In 1D systems, it is the plasmonic resonance which dominates for low concentrations [Fig. 5(d)]. Mixed modes appear with increasing carrier concentration, and they successively transform into the geometrical modes at high concentrations.

The 2D systems are specific as both geometrical and plasmonic resonances depend on the carrier concentration in the same manner: the mixing between geometrical and plasmonic resonances keeps the square-root dependence of the resonant frequency, only the mixed resonance frequencies are systematically scaled [shifted in the log scale in Fig. 5(e)], and their line shape is altered. The mixing can be better understood when the density of nanosheets η_2 is varied (Fig. 9): the geometrical resonances exist at small density, and they are progressively converted into a single plasmonic resonance at higher densities η_2 .

The crossing of the first geometrical branch with the plasmonic branch occurs for carrier density for which the frequencies of the plasmonic and geometrical resonance are equal; this density reads

$$n_{\text{cross}} = \frac{\eta_1 m l^2}{\epsilon_1} (1-s) \frac{4e_0^2}{\pi^4 \hbar^2 \epsilon_0} \quad \text{for 1D nanostructures,} \quad (15)$$

$$n_{\text{cross}} = \left(\frac{\epsilon_1}{m l^2} \right)^3 \frac{1}{(1-s)^3} \frac{9\pi^{10} \hbar^6 \epsilon_0^3}{e_0^6} \quad \text{for 3D nanostructures.} \quad (16)$$

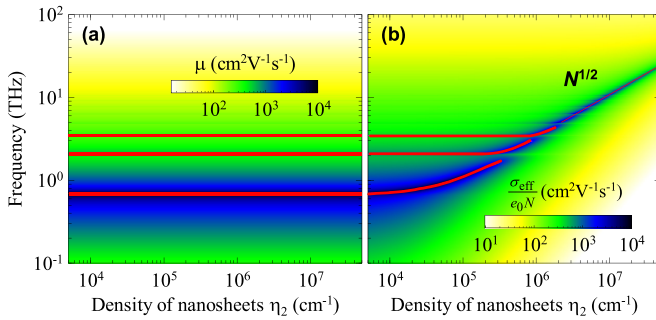


FIG. 9. Response of 2D electron gas as a function of the density of nanosheets η_2 . (a) The mobility spectrum is independent of the density of nanosheets η_2 . (it depends only on the sheet carrier density n). (b) Effective conductivity of mutually isolated nanostructures forming the brick-wall structure shown in Fig. 7. Solid red lines serve as a guide for the eye to indicate the behavior of three lowest resonances: The parts of the curves following the $N^{1/2}$ trend represent the plasmonic resonance whereas the horizontal parts (independent of η_2) represent the geometrical resonances. Parameters: $l = 300$ nm, $n = 10^{12}$ cm $^{-2}$, $s = 0.5$, $E_F = 0.2$ eV, and $\tau_s = 10$ ps.

These expressions show that there is a large parameter space (altogether represented by the parameters m , s , l , ε_1 , and η_1) controlling the crossover. This permits finding a suitable material and conditions to tune the crossover carrier density and frequency as desired. In particular, it allows us to experimentally reach the regimes below, close to, and above the crossover carrier density while satisfying the assumptions used in the semiclassical description. Note also that for proposing real experiments one has to carefully consider the carrier-density and temperature dependence of the scattering time. This time has to be sufficiently long to resolve the target resonance(s), and at the same time short enough to avoid dominance of quantum phenomena.

V. CONCLUSIONS

In summary, we have calculated the terahertz conductivity spectra of charges moving classically in infinite rectangular potential wells. Structures containing degenerate electron gases exhibit specific spectral features—geometrical resonances—associated with characteristic bouncing frequencies and also with higher harmonics due to anharmonic nature of charge thermal trajectories. Mutually isolated nanostructures support the formation of plasmonic resonance, which couples with the geometrical resonances. Whereas the plasmonic resonance in 3D nanostructures dominates only at high carrier densities, in one dimension it dominates only at low carrier concentrations. In 2D nanostructures, the plasmonic and geometrical resonances remain coupled independently of the carrier density. Observation of these resonances requires structures with bulk scattering times exceeding one half of the round-trip time. The response of confined nondegenerate electron gases is characterized by a single broad absorption band even in the absence of bulk scattering and inhomogeneous broadening. Quantum-mechanical calculations confirmed that the semiclassical approach is well applicable for the qualitative understanding of the underlying physical effects responsible for the terahertz and multiterahertz response of larger nanostructures.

ACKNOWLEDGMENTS

We acknowledge financial support by the Czech Science Foundation (Project No. 17-04412S) and by Operational Program Research, Development and Education financed by European Structural and Investment Funds and the Czech Ministry of Education, Youth and Sports (Project No. SOLID21—CZ.02.1.01/0.0/0.0/16_019/0000760). We also acknowledge Petr Kužel for fruitful discussions.

- [1] R. R. Gerhardt, D. Weiss, and K. von Klitzing, *Phys. Rev. Lett.* **62**, 1173 (1989).
- [2] R. A. Deutschmann, W. Wegscheider, M. Rother, M. Bichler, G. Abstreiter, C. Albrecht, and J. H. Smet, *Phys. Rev. Lett.* **86**, 1857 (2001).
- [3] A. Kawabata and R. Kubo, *J. Phys. Soc. Jpn.* **21**, 1765 (1966).
- [4] E. J. Austin and M. Wilkinson, *J. Phys.: Condens. Matter.* **5**, 8461 (1993).
- [5] H. Němec, V. Zajac, I. Rychetský, D. Fattakhova-Rohlfing, B. Mandlmeier, T. Bein, Z. Mics, and P. Kužel, *IEEE Trans. THz Science Technol.* **3**, 302 (2013).
- [6] M. C. Beard, G. M. Turner, and C. A. Schmuttenmaer, *Nano Lett.* **2**, 983 (2002).
- [7] D. G. Cooke, A. Meldrum, and P. Uhd Jepsen, *Appl. Phys. Lett.* **101**, 211107 (2012).
- [8] H. J. Joyce, C. J. Docherty, Q. Dao, H. H. Tan, C. Jagadish, J. Lloyd-Hughes, L. M. Herz, and M. B. Johnston, *Nanotechnology* **24**, 214006 (2013).
- [9] F. A. Hegmann, O. Ostroverkhova, and D. G. Cooke, in *Photophysics of Molecular Materials*, edited by G. Lanzani (Wiley-VCH, Weinheim, 2006).
- [10] J. Lloyd-Hughes, S. K. E. Merchant, L. Sirbu, I. M. Tiginyanu, and M. B. Johnston, *Phys. Rev. B* **78**, 085320 (2008).
- [11] N. V. Smith, *Phys. Rev. B* **64**, 155106 (2001).
- [12] M. Wilkinson and E. J. Austin, *J. Phys.: Condens. Matter.* **6**, 4153 (1994).
- [13] B. Mehlig and K. Richter, *Phys. Rev. Lett.* **80**, 1936 (1998).
- [14] B. Mehlig, D. Boosé, and K. Müller, *Phys. Rev. Lett.* **75**, 57 (1995).
- [15] B. G. L. Jager, S. Wimmer, A. Lorke, J. P. Kotthaus, W. Wegscheider, and M. Bichler, *Phys. Rev. B* **63**, 045315 (2001).
- [16] L. Nádvořík, M. Orlita, N. A. Goncharuk, L. Smrčka, V. Novák, V. Jurka, K. Hruška, Z. Výborný, Z. R. Wasilewski, M. Potemski, and K. Výborný, *New. J. Phys.* **14**, 053002 (2012).
- [17] H. Němec, P. Kužel, and V. Sundström, *Phys. Rev. B* **79**, 115309 (2009).
- [18] T. L. Cocker, D. Baillie, M. Buruma, L. V. Titova, R. D. Sydora, F. Marsiglio, and F. A. Hegmann, *Phys. Rev. B* **96**, 205439 (2017).

- [19] J. Lloyd-Hughes and T.-I. Jeon, *J. Infrared Milli. Terahz. Waves* **33**, 871 (2012).
- [20] T. Ostatnický, V. Pushkarev, H. Němec, and P. Kužel, *Phys. Rev. B* **97**, 085426 (2018).
- [21] R. Kubo, *J. Phys. Soc. Jpn.* **12**, 570 (1957).
- [22] C. M. Wolfe, G. E. Stillman, and T. L. Lindley, *J. Appl. Phys.* **41**, 3088 (1970).
- [23] C. S. Ponseca, Jr., H. Němec, J. Wallentin, N. Anttu, J. P. Beech, A. Iqbal, M. Borgström, M.-E. Pistol, L. Samuelson, and A. Yartsev, *Phys. Rev. B* **90**, 085405 (2014).
- [24] C. Kadlec, F. Kadlec, P. Kužel, K. Blary, and P. Mounaix, *Opt. Lett.* **33**, 2275 (2008).
- [25] H. K. Nienhuys and V. Sundström, *Appl. Phys. Lett.* **87**, 012101 (2005).